Additive Manufacturing 42 (2021) 101983

Contents lists available at ScienceDirect

Additive Manufacturing

journal homepage: www.elsevier.com/locate/addma

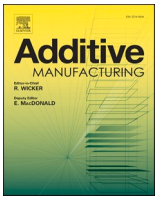

Estimations of the effective Young's modulus of specimens prepared by fused filament fabrication☆

Lichen Fang [a], Yishu Yan [a], Ojaswi Agarwal [a], Jonathan E. Seppala [b], Kalman D. Migler [b], Thao D. Nguyen [a], Sung Hoon Kang [a,*]

[a] Department of Mechanical Engineering and Hopkins Extreme Materials Institute, Johns Hopkins University, Baltimore, MD 21218, USA
[b] Materials Science and Engineering Division, National Institute of Standards and Technology, Gaithersburg, MD 20899, USA

ARTICLE INFO

Keywords:
Extrusion
Fused filament fabrication
Tension test
Effective Young's modulus

ABSTRACT

The elastic response of homogeneous isotropic materials is most commonly represented by their Young's modulus (E), but geometric variability associated with additive manufacturing results in materials that are neither homogeneous nor isotropic. Here we investigated methods to estimate the effective elastic modulus (E_{eff}) of samples fabricated by fused filament fabrication. We conducted finite element analysis (FEA) on printed samples based on material properties and CT-scanned geometries. The analysis revealed how the layer structure of a specimen altered the internal stress distribution and the resulting E_{eff}. We also investigated different empirical methods to estimate E_{eff} as guides. We envision the findings from our study can provide guidelines for modulus estimation of as-printed specimens, with the potential of applying to other extrusion-based additive manufacturing technologies.

1. Introduction

Additive manufacturing (AM) is one of the latest revolutions in manufacturing technology. AM allows users with minimal training to easily convert their digital models into physical objects and opens up more design freedom for making optimized 3D structures [1]. Among the AM technologies, material extrusion-based AM [2] represents the most common category of AM method, which extrudes material feedstock along the designated contour to form 3D shapes. Depending on the material types and extrusion mechanisms, there are several different AM methods under this category, including direct ink writing (DIW) and fused filament fabrication (FFF) [3]. However, due to the fundamental limitation of material extrusion processes, all these methods share the same setback of non-uniform cross-section geometries [4]. Specifically, most as-extruded materials have circular cross-sections. The bonding region between two adjacent extrudates is narrower when stacked layer-by-layer, significantly influencing the overall mechanical properties [5].

There have been many studies investigating the mechanical performance of parts made by material extrusion AM in the past. Most of the works focused on studying the effects on tensile strength by varying processing parameters, including geometrical parameters, thermal profiles, deposition rates, and tool paths [6–12]. Besides tensile strength, other mechanical measurements like failure modes, peeling tests, and Grave tear tests have also been reported [13–16]. These results show how the specimens fail upon normal and shear loadings from different directions. Nevertheless, only a few studies have quantitatively investigated the elastic response upon changing printing conditions.

The Young's modulus is an important material property used for material design and selection. It is essential when considering the elastic response of a printed thin wall, which has a highly non-uniform cross-section geometry and therein very different mechanical performance [17]. Among the few studies that have investigated the elastic behavior of printed parts, most of them concluded that the tool path [18–21] and infill density [22,23] are the critical factors that impact the modulus, as they could influence the effective loading area. Additionally, Park et al. [24] also stated that the geometrical non-uniformity brought by printer mechanical inaccuracy could further decrease the modulus as well. However, a comprehensive understanding and prediction of the process-geometry-modulus relationship is still needed.

To address this issue, the AM community has been calling for Young's modulus test standards that could account for the modulus

☆ Official contribution from the National Institute of Standards and Technology; not subject to copyright in the United States.

* Corresponding author.
E-mail address: shkang@jhu.edu (S.H. Kang).

https://doi.org/10.1016/j.addma.2021.101983
Received 17 December 2020; Received in revised form 5 March 2021; Accepted 23 March 2021
Available online 5 April 2021

change brought by the printing process [25]. Let's consider a typical tensile test procedure. The force is normalized by the cross-section area (of the standard dogbone tensile specimen) to get the stress, then from stress we could divide it by strain and obtain the elastic modulus. Here we call this "effective Young's modulus (E_{eff})" since it reflects the combined effects of the material's intrinsic modulus (E) and printed geometry. As intrinsic modulus could change after processing and the printed geometry has a non-uniform cross-section dimensions, the estimation of effective Young's modulus is very challenging, especially when a full cross-section geometry is not available.

This study investigated different ways to estimate the effective Young's modulus from measured intrinsic modulus and geometries. From micro-CT scanned digital model and simplified cross-section geometries, finite element analysis (FEA) was performed and shown to predict the effective Young's modulus. Moreover, we evaluated different empirical methods to estimate E_{eff} based on cross-section geometry and stress distribution by comparing them with experimental results as guides for modulus estimation of as-printed specimens.

2. Materials and methods

2.1. Material and equipment

Fig. 1 shows a typical geometry of extrusion-based AM tensile specimens, where the cross-section is non-uniform, and the width varies at different locations along the length of the specimen. To investigate the elastic response of specimens prepared by FFF, we fabricated multiple specimens, then performed tensile tests and finite element simulations. In this study, Ultimaker[1] bisphenol-A-polycarbonate (PC) filament was used to print all the specimens. All filaments were dried at approximately 100 °C for 1 h prior to printing to remove moisture and minimize specimen porosity. Specimens were printed using a LulzBot TAZ 6 printer with an acrylic enclosure (Printed Solid, Inc.). By pumping dry compressed air into the enclosure, the environmental humidity was kept below 10 % RH to further minimize the effect of moisture on the mechanical properties of the printed material. After printing, the as-fabricated box shapes were laser cut into dogbone tensile specimens using VLS 6.60 laser cutter.

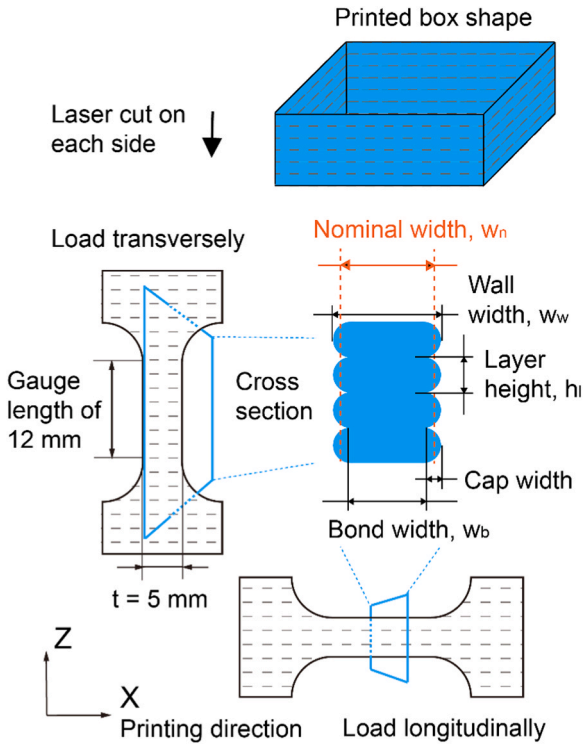

Fig. 1. Schematics of the printed box-shape specimens, and the laser-cut tensile specimens in both testing directions: one loading along printing direction X (longitudinal), the other loading along layer stacking direction Z (transverse).

2.2. FFF processing conditions

Multiple thin wall specimens were printed using three different yet commonly used layer heights: 0.15 mm, 0.30 mm, and 0.45 mm, while other parameters were kept constant (nozzle temperature = 280 °C, print speed = 10 mm/s, build plate temperature = 115 °C, flow index: 100 %). Here the 100 % flow index indicates the printing system has been calibrated to have actual extruded volume equals to the designed volume, where designed volume is the product of layer height, nominal width, print speed and time; extruded volume is the product of nozzle extruding area, extrusion speed and time. Each thin wall represents a stack of single extrudates and within each layer there is only one continuous extrudate deposited.

2.3. Geometrical characterizations

After printing, the specimens were scanned by Bruker Skyscan 1172 Micro-CT scanner with a spatial resolution of 4.87 μm/pixel (results were calibrated following the procedure of a previous study [26]). The scanned models were imported into MATLAB for further image analysis, which facilitated spatial measurements of each layer. As defined in Fig. 1, wall width and bond width were extracted by identifying edges and counting pixels across the corresponding sections.

During the extrusion process, the as-extruded material is confined by the substrate and the extruder, forming the parallel top and bottom edges; while in the horizontal direction, the molten material could form rounded cap regions, as Fig. 2(a) (top) shows. Then, we quantified the curvature of the caps and plotted the results in Fig. 2(b). We found the radius of curvature is slightly larger than half of the layer height, indicating the cap shape is not exactly a semi-circle. Inspired by those results, we propose a simplified representation of the cross-section shape, as plotted in Fig. 2(a) (bottom): the central confined region is a rectangle, the cap regions are two semi-ellipse with (wall width − bond width) and layer height as the major and minor axis of the ellipse, respectively. This gives the relationship that the cap width equals half of the difference between wall width and bond width. As those dimensions are relatively easy to measure, this simplification provides a straightforward way to estimate the cross-section shape, considering the difficulty and steep costs of performing micro-CT scans. (See section S1 of Supplemantary materials for details.).

2.4. Numerical simulations

Based on both scanned geometry and simplified geometry, simulations of the tensile tests were conducted with the commercial finite

[1] Certain commercial equipment, instruments, or materials are identified in this paper in order to specify the experimental procedure adequately. Such identification is not intended to imply recommendation or endorsement by the National Institute of Standards and Technology, nor is it intended to imply that the materials or equipment identified are necessarily the best available for the purpose.

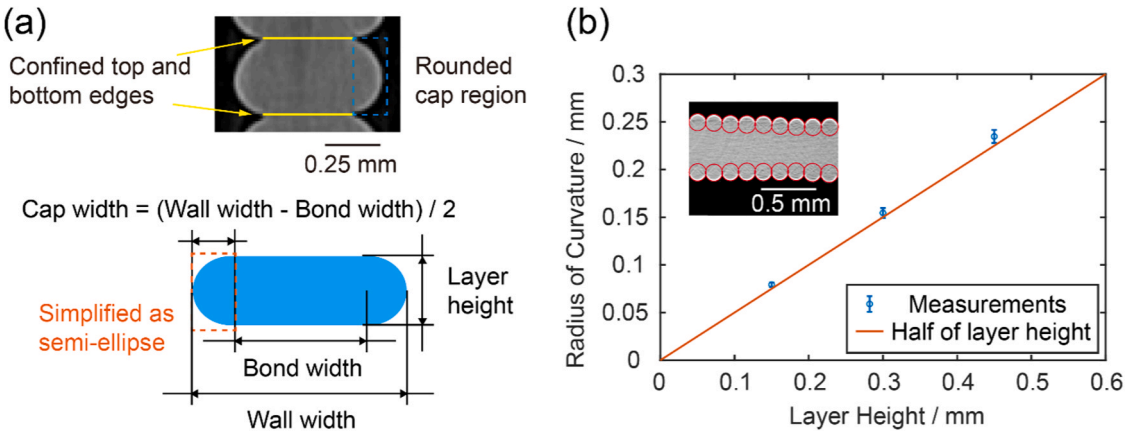

Fig. 2. (a) Simplification of the cross-section geometry, which is broken down into a rectangle plus two semi-elliptical caps; (b) Measurement of cap region's curvature, the radius of curvature is slightly higher than half of the layer height, indicating the cap shape is not exactly circular. Error bars are defined by the standard deviation of measurements on 30 bonds.

element package Abaqus/Standard. As Fig. 3(a) shows, the section was given by either scanned or simplified geometry, while the thickness is 5 mm, which equals to the gauge width of the dogbone tensile specimen. The bottom surface was constrained in the loading direction, and the bottom-left node was fixed in all directions. A small displacement loading was applied on a reference point coupled to the top surface, and all other boundaries were set as free to simulate the uniaxial tensile condition. The 8-node linear brick with hourglass control and reduced integration element (C3D8R) was used in the full 3D simulations. Since we are investigating the elastic properties of tensile specimens, linear-elastic material properties were applied in simulations. It is known that FFF process may generate anisotropy in the exterior shell of the extrudates due to the high shear within the extruder, and the welding interfaces between two extrudates could also have different properties. However, considering the thin thickness of those interfaces, they will have minimal impact to the overall modulus. So, it is reasonable to assume the entire body has same linear elastic properties. To get the intrinsic modulus, uniaxial tensile tests were performed on 0.5 mm diameter free-hung filament extruded from the printer nozzle, using the same printing parameters. The Young's modulus of the as-printed filament was measured to be 1.82 GPa ± 0.05 GPa (standard deviation given by 5 measurements), which was applied to simulation together with the Poisson's ratio of 0.35. After the simulations, the reaction force on the reference point was extracted, which is equivalent to the reaction force on the top-loading surface.

2.5. Mechanical characterizations

To validate the simulations, we also performed mechanical tests on printed samples. 38 mm by 15 mm dogbone tensile specimens were prepared using VLS 6.60 laser cutter, which follow the ASTM D1708 standard and have 12 mm by 5 mm gauge areas. For each set of layer heights, at least 10 tensile specimens were fabricated and tested, with 5 specimens loaded along printing direction (longitudinal test) and 5 specimens loaded perpendicular to printing direction (transverse test), as shown in Fig. 1. Variability is presented as the standard deviation of the 5 samples. Quasi-static uniaxial tensile tests (with load rate of 0.01 mm/s) were then conducted using an Instron ElectroPuls E1000 tester. During the tests, the deformation within the gauge area was recorded and captured by a Canon EOS 80D digital single-lens reflex (DSLR) camera. (See section **S2** of Supplemantary Materials for more details.).

3. Results and discussions

3.1. Comparisons of simulations with experiments for different layer heights

By comparing the effective Young's modulus obtained from simulations and experiments, we find the simulations based on CT-scanned profiles can successfully emulate the specimens' measured effective Young's modulus, as Fig. 3(b) shows. This further confirms that

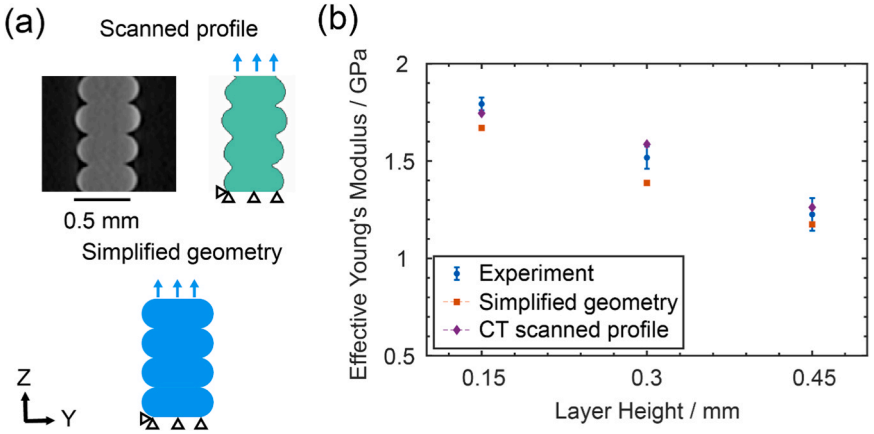

Fig. 3. (a) Finite element analysis setup based on both CT-scanned profile and simplified geometry model; (b) Comparison between measured Young's modulus in transverse tests and the corresponding predictions from finite element method. The error bars are from standard deviations of data obtained from 5 measurements.

geometry and intrinsic modulus change contribute together to the effective Young's modulus change, which could be accurately estimated by considering both factors. However, as the intrinsic modulus change is only 3 % (raw filament: 1.87 GPa; after extrusion: 1.82 GPa), geometry shall be the primary cause for the change. Meanwhile, simulations based on scanned geometry matches better with the experiments, while simulations based on the simplified geometry (a stack of layers described in Fig. 2(a)) also has satisfactory accuracy, which provides a sufficient method to identify the cross-section shape when CT is not available. Generally, there is a trend of decreasing effective Young's modulus with increasing layer height. This aligns with our previous geometrical characterization that the cap radius of curvature has linear relationship with the layer height. With larger layer height, the caps will also be larger and makes the bonding area to be smaller, which results in a reduction in the effective Young's modulus.

Then, we analyzed the stress distribution within the tensile specimens at 0.3 mm layer height (Fig. 4). From the simulation results of scanned geometry, the stress in YY and YZ directions is less than 15 % of the stress in the ZZ direction. For the normal stress along the loading direction (ZZ), the stress within bond width is almost uniform, except a few stress concentration regions at linking points between adjacent layers. Meanwhile, the stress in ZZ direction drops significantly out of the bond width region. At the very far edges in the caps, compressive stress is observed. Quantitatively, the effective modulus within caps is around 30 % of the material's intrinsic Young's modulus: by integrating the loading direction normal stress (S_{ZZ}) across the cap regions, we found that the cap region can provide an average of 30 % of stiffness per unit width compared to the bond region.

3.2. *Evaluation of different experimental methods to estimate the effective Young's modulus*

Based on the analysis of stress distribution, multiple methods were proposed and evaluated to estimate the effective Young's modulus of the 3D-printed specimens. The effective modulus links the overall mechanical performance with dimensions of specimens and material intrinsic modulus, as shown in Table 1. In experiments, the E_{eff} equals force divided by the nominal cross section area and strain.

E is the material intrinsic modulus of 1.82 GPa, w_n is the nominal width of 0.5 mm, w_b is the bond width, w_w is the wall width, cap width is $(w_w - w_b)/2$, l_h is the layer height; for the analytical averaging method, w (z) stands for the real width at each z location.

Among these methods, the E_{eff}^{mat} and E_{eff}^{wall} are the easiest to get: the $E_{eff}^{nominal}$ is simply assuming there is no cap and the geometry is identical to the digital design; while the wall width w_w in E_{eff}^{wall} could be measured by a caliper. For the E_{eff}^{bond} method, as the majority of the positive tensile normal stress S_{zz} would be distributed within the narrowest neck - bond width (Fig. 4), it is natural to assume these regions make significant contributions to the overall tensile properties. Another method $E_{eff}^{averaging}$ would be discretizing the specimen into thin slices, then consider them as a series of springs and integrate their compliance. The key assumption here is each slice remains planar after deformation, and there is no shear or bending stress. Finally, the $E_{eff}^{bond+0.6cap}$ method is evaluated, which considers a factor based on the stress distribution results from the numerical simulation: in this study, simulation results suggest using bond width plus 0.6 times cap width (half of the difference between wall width and bond width, see Fig. 1). Given the CT test data shown in Fig. 2, we know that the cap width is approximately equal to half of the layer

Table 1
Description of proposed estimation methods.

Method	Equation of effective Young's modulus
Material instrinsic modulus	$E_{eff}^{mat} = E$
Wall width	$E_{eff}^{wall} = w_w E/w_n$
Bond width	$E_{eff}^{bond} = w_b E/w_n$
Averaging	$E_{eff}^{averaging} = \int w(z)E/w_n \, dz$
Bond width + 60 % cap width	$E_{eff}^{bond+0.6cap} = (w_b + 0.6 \times (w_w - w_b)/2) \times E/w_n$
Wall width - 70 % layer height	$E_{eff}^{wall-0.7h_l} = (w_w - 0.7 \times h_l) \times E/w_n$

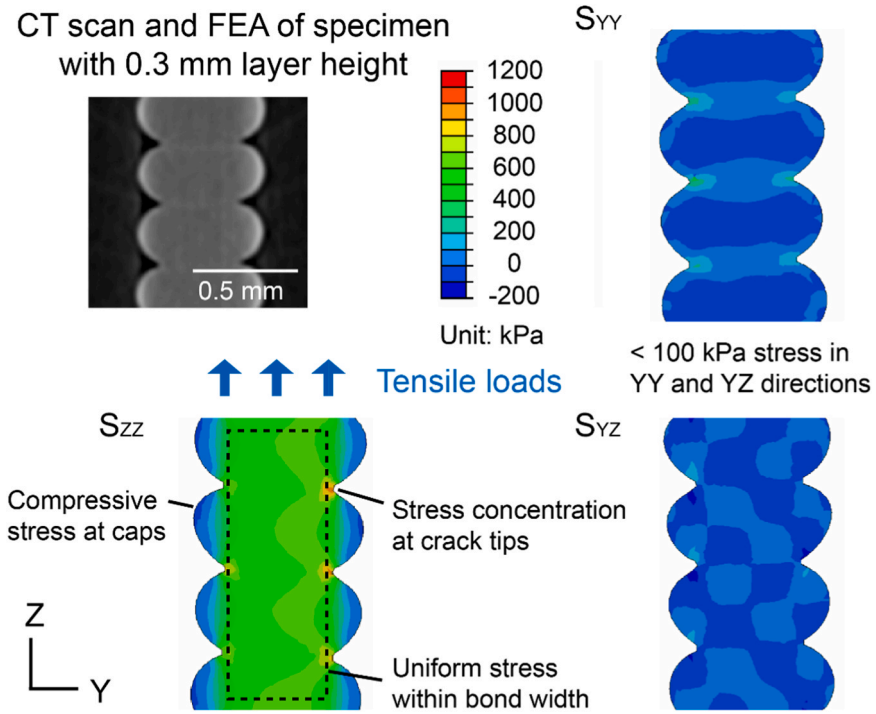

Fig. 4. Finite element simulation of tensile tests along transverse direction of specimen with 0.3 mm layer height. The stress distribution in the midplane of the specimen is illustrated.

Table 2
Comparison of the estimated effective moduli for 0.45 mm layer height and the measured value (1.23 GPa ± 0.08 GPa). Deviation is calculated by (Estimation - Measurement) / Measurement *100 %.

Method	Estimated modulus at $h_l = 0.45$ mm (GPa)	Deviation (%)
Measurement	1.23 ± 0.08	N/A
Material instrinsic modulus E_{eff}^{mat}	1.82 ± 0.05	+ 48.0
Wall width E_{eff}^{wall}	2.27 ± 0.06	+ 84.6
Bond width E_{eff}^{bond}	0.90 ± 0.02	-26.8
Averaging $E_{eff}^{averaging}$	1.72 ± 0.05	+ 39.8
Bond width + 60 % cap width $E_{eff}^{bond+0.6cap}$	1.31 ± 0.04	+ 6.5
Wall width - 70 % layer height $E_{eff}^{wall-0.7h_l}$	1.12 ± 0.03	-8.9

height, so that 'bond width + 60 % cap width' could be approximated to 'wall width - 70 % layer height', which gives the $E_{eff}^{wall-0.7h_l}$ as Eq. (1):

$$w_b + 0.6 \times (w_w - w_b)/2 = 0.3w_w + 0.7w_b = w_w - 0.7 \times (w_w - w_b) \approx w_w - 0.7 \times h_l \quad (1)$$

where $w_w - w_b = 2 \times$ cap width $\approx h_l$.

For longitudinal loaded specimens, there is no significant change in the cross-section areas along the loading direction, and there is only less than 2 % variation brought by the printing process. As a result, their effective modulus may be estimated by dividing the stress by the sample cross-section area. To be noted here, this creates anisotropic stiffness behavior in general FFF specimens. For larger scale parts that have different raster angles or under mixed loading conditions, FEA simulations are recommended to get precise estimations.

The comparison between different estimation methods are shown in Table 2 and Fig. 5, where the effective modulus is estimated based on each method, and the experimentally measured value is denoted as solid black dots. Generally, all methods work better at a thinner layer height (less geometry variation), while at a thicker layer height, the deviation is higher.

Both E_{eff}^{mat} and E_{eff}^{wall} overestimated the effective Young's modulus, as both options do not account for the narrower necks, which significantly reduces the load-bearing capability. For the E_{eff}^{bond}, though the simulation supports our hypothesis that the positive normal stress mainly distributes within the neck region, using bond width still underestimates the effective modulus. This means that the cap region has significant contributions to the effective modulus. Similarly, though simulations show the stresses in YY and YZ directions are small, there are still up to 40 % deviations between the $E_{eff}^{averaging}$ and experimental results. This suggests that the assumption of plane sections remain plane is not true: the small YY and YZ stresses still affect the overall load-bearing capability.

Finally, both the $E_{eff}^{bond+0.6cap}$ and $E_{eff}^{wall-0.7h_l}$ gave consistent estimations of the effective Young's modulus at all tested layer heights and have the lowest standard deviation (± 10 % deviation). While $E_{eff}^{wall-0.7h_l}$ has relatively lower accuracy than $E_{eff}^{bond+0.6cap}$, this approach does not require CT measurements of the bond width, which makes it easier to apply in engineering practices. From this result, we learned that while the bond width contributes most to the overall stiffness, the cap region has around 30 % modulus compared to that of a solid cubic part with the same dimensions; both regions need to be counted to get an accurate estimation. Moreover, since the relationship between intrinsic modulus, geometry, and effective modulus is found, we can estimate the intrinsic modulus from the exterior dimension and effective modulus of printed specimens, which will be helpful when there is a significant change in intrinsic modulus before and after printing. However, it must be noted that this work is based on a geometry of single-extrudate wall while most of FFF parts consist of walls with multiple extrudates. As a result, the rounded caps are likely to overlap and weld with each other, resulting in more complex bond areas within a solid body. The modulus estimation of such structures will be more complicated. Macroscopically, the as-fabricated structure will be a solid body with multiple voids, that each void is formed by the uncovered space between adjacent extrudates.

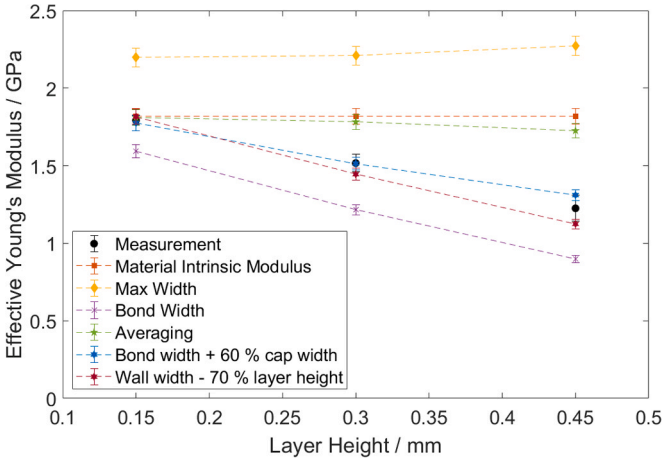

Fig. 5. The estimation of effective modulus E_{eff} using different methods, error bars are from the uncertainty in measuring the intrinsic modulus E. The experimentally measured E_{eff} values are denoted as solid black dots; the error bars are from standard deviations of data obtained from 5 measurements.

Microscopically, the melt flow and welding between extrudates will also create anisotropy in both mechanical stiffness and welding strength.

4. Summary and conclusions

In this work, we investigated methods to estimate the effective elastic modulus (E_{eff}) of samples fabricated by fused filament fabrication. We conducted finite element analysis (FEA) on printed samples based on material properties and CT-scanned geometries to find the relationship between material intrinsic modulus, printed geometry, and the effective elastic modulus. The analysis revealed how the layer structure of a specimen altered the internal stress distribution and the resulting E_{eff}. Importantly, the simulations based on CT-scanned profiles could successfully emulate the specimens' effective Young's modulus. In lieu of the method based on CT scans and FEA, we have also evaluated different empirical methods based on the material intrinsic modulus value and the exterior dimensions of printed specimens. We have found that the method derived from the stress distribution information from simulations shows good estimation accuracy with less than 10 % error for three different tested layer heights. We envision the findings from our study will provide guidelines for the effective elastic modulus estimation of as-printed specimens, with the potential of applying to other extrusion-based AM technologies since the layer-by-layer structure is widely found in extrusion-based AM parts.

CRediT authorship contribution statement

Lichen Fang: Methodology, Formal analysis, Investigation, Visualization, Writing – Original Draft, Review & Editing, **Yishu Yan:** Methodology, Formal analysis, Visualization, **Ojaswi Agarwal:** Methodology, Formal analysis, Investigation, Visualization, Writing - Review & Editing, **Jonathan E. Seppala:** Methodology, Investigation, Writing - Review & Editing, **Kalman D. Migler:** Investigation, Writing - Review & Editing, **Thao D. Nguyen:** Funding acquisition, Supervision, **Sung Hoon Kang:** Funding acquisition, Project administration, Conceptualization, Methodology, Investigation, Supervision, Writing – Original Draft, Review & Editing.

Declaration of Competing Interest

The authors declare that they have no known competing financial interests or personal relationships that could have appeared to influence the work reported in this paper.

Acknowledgements

We would like to acknowledge the partial support of the National Science Foundation (DMREF-1628974), and the start-up fund from the Whiting School of Engineering at Johns Hopkins University. We would like to thank Prof. Stavros Gaitanaros and Ms. Sirui Bi for allowing us to use their micro-CT machine and providing help. We also would like to thank Prof. Peter Olmsted, Prof. Mark O. Robbins, Mr. Zheliang Wang and Mr. Marco Galvani Cunha for helpful comments and suggestions regarding this study.

Appendix A. Supporting information

Supplementary data associated with this article can be found in the online version at doi:10.1016/j.addma.2021.101983.

References

[1] H. Lipson, M. Kurman, Fabricated: The New World of 3D Printing, John Wiley & Sons, 2013.
[2] ISO 17296–2:2015 Additive Manufacturing — General Principles — Part 2: Overview of Process Categories and Feedstock, International Organization for Standardization.
[3] K. Rane, M. Strano, A comprehensive review of extrusion-based additive manufacturing processes for rapid production of metallic and ceramic parts, Adv. Manuf. 7 (2019) 155–173.
[4] B.N. Turner, R. Strong, S.A. Gold, A review of melt extrusion additive manufacturing processes: I. Process design and modeling, Rapid Prototyp. J. 20 (2014) 192–204.
[5] B.N. Turner, S.A. Gold, A review of melt extrusion additive manufacturing processes: II. Materials, dimensional accuracy, and surface roughness, Rapid Prototyp. J. 21 (2015) 250–261.
[6] Q. Sun, G.M. Rizvi, C.T. Bellehumeur, P. Gu, Effect of processing conditions on the bonding quality of FDM polymer filaments, Rapid Prototyp. J. 14 (2008) 72–80.
[7] A.T. Alsharhan, T. Centea, S.K. Gupta, in: American Society of Mechanical Engineers Digital Collection, 2017. https://asmedigitalcollection.asme.org/MSEC/proceedings-abstract/MSEC2017/50732/V002T01A016/269483.
[8] J.E. Seppala, S.H. Han, K.E. Hillgartner, C.S. Davis, K.B. Migler, Weld formation during material extrusion additive manufacturing, Soft Matter 13 (2017) 6761–6769.
[9] M. Spoerk, C. Savandaiah, F. Arbeiter, G. Traxler, L. Cardon, C. Holzer, J. Sapkota, Anisotropic properties of oriented short carbon fibre filled polypropylene parts fabricated by extrusion-based additive manufacturing, Compos. Part A Appl. Sci. Manuf. 113 (2018) 95–104.
[10] D.A. Anderegg, H.A. Bryant, D.C. Ruffin, S.M. Skrip, J.J. Fallon, E.L. Gilmer, M. J. Bortner, In-situ monitoring of polymer flow temperature and pressure in extrusion based additive manufacturing, Addit. Manuf. 26 (2019) 76–83.
[11] T.J. Coogan, D.O. Kazmer, Bond and part strength in fused deposition modeling, Rapid Prototyp. J. 23 (2017) 414–422.
[12] Y. Jin, Y. He, J. Fu, W. Gan, Z. Lin, Optimization of tool-path generation for material extrusion-based additive manufacturing technology, Addit. Manuf. 1–4 (2014) 32–47.
[13] J.C. Riddick, M.A. Haile, R.V. Wahlde, D.P. Cole, O. Bamiduro, T.E. Johnson, Fractographic analysis of tensile failure of acrylonitrile-butadiene-styrene fabricated by fused deposition modeling, Addit. Manuf. 11 (2016) 49–59.
[14] R. Hashemi Sanatgar, C. Campagne, V. Nierstrasz, Investigation of the adhesion properties of direct 3D printing of polymers and nanocomposites on textiles: effect of FDM printing process parameters, Appl. Surf. Sci. 403 (2017) 551–563.
[15] J. Kotlinski, Mechanical properties of commercial rapid prototyping materials, Rapid Prototyp. J. 20 (2014) 499–510.
[16] C.S. Davis, K.E. Hillgartner, S.H. Han, J.E. Seppala, Mechanical strength of welding zones produced by polymer extrusion additive manufacturing, Addit. Manuf. 16 (2017) 162–166.
[17] T. Letcher, B. Rankouhi, S. Javadpour, in: American Society of Mechanical Engineers Digital Collection, 2016. https://asmedigitalcollection.asme.org/IMECE/proceedings-abstract/IMECE2015/V02AT02A018/260510.
[18] M. Bertoldi, M. Yardimci, C.M. Pistor, S.I. Guceri, G. Sala, in: International Solid Freeform Fabrication Symposium, 1998. https://repositories.lib.utexas.edu/handle/2152/73496.
[19] B.M. Tymrak, M. Kreiger, J.M. Pearce, Mechanical properties of components fabricated with open-source 3-D printers under realistic environmental conditions, Mater. Des. 58 (2014) 242–246.
[20] A. Lanzotti, M. Grasso, G. Staiano, M. Martorelli, The impact of process parameters on mechanical properties of parts fabricated in PLA with an open-source 3-D printer, Rapid Prototyp. J. 21 (2015) 604–617.
[21] C.E. Duty, V. Kunc, B. Compton, B. Post, D. Erdman, R. Smith, R. Lind, P. Lloyd, L. Love, Structure and mechanical behavior of Big Area Additive Manufacturing (BAAM) materials, Rapid Prototyp. J. 23 (2017) 181–189.
[22] X. Deng, Z. Zeng, B. Peng, S. Yan, W. Ke, Mechanical properties optimization of poly-ether-ether-ketone via fused deposition modeling, Materials 11 (2018) 216.
[23] T. Webbe Kerekes, H. Lim, W.Y. Joe, G.J. Yun, Characterization of process–deformation/damage property relationship of fused deposition modeling (FDM) 3D-printed specimens, Addit. Manuf. 25 (2019) 532–544.
[24] S.-I. Park, D.W. Rosen, S. Choi, C.E. Duty, Effective mechanical properties of lattice material fabricated by material extrusion additive manufacturing, Addit. Manuf. 1–4 (2014) 12–23.
[25] D. Popescu, A. Zapciu, C. Amza, F. Baciu, R. Marinescu, FDM process parameters influence over the mechanical properties of polymer specimens: a review, Polym. Test. 69 (2018) 157–166.
[26] L. Fang, Y. Yan, O. Agarwal, J.E. Seppala, K.J. Hemker, S.H. Kang, Processing-structure-property relationships of bisphenol-A-polycarbonate samples prepared by fused filament fabrication, Addit. Manuf. 35 (2020), 101285.